J Mater Sci (2010) 45:5786–5794
DOI 10.1007/s10853-010-4652-8

ZnO nanoparticles supported on mesoporous MCM-41 and SBA-15: a comparative physicochemical and photocatalytic study

G. D. Mihai · V. Meynen · M. Mertens · N. Bilba · P. Cool · E. F. Vansant

Received: 15 March 2010 / Accepted: 21 May 2010 / Published online: 8 June 2010

Abstract A simple solvothermal impregnation method was used to prepare ZnO nanoparticles supported on MCM-41 and SBA-15. X-ray powder diffraction, N_2 adsorption–desorption, Electron Probe Micro Analysis (EPMA), and UV–vis spectroscopy were used to characterize the prepared materials. The influence of the ZnO loading of different supports on the structural characteristics and the photocatalytic activity toward degradation of methylene blue in water under ultraviolet irradiation were investigated. Wide angle X-ray diffraction and UV–vis Diffuse Reflectance confirmed the existence of ZnO phase. A much smaller influence of impregnation with ethanolic zinc salt solution on the porosity was observed for SBA-15 compared with MCM-41. Finally, the adsorption and photocatalytic activity of the ZnO/mesoporous materials depend on porous characteristics of the support materials.

Introduction

Owing to its *n*-type II–VI semiconductor properties such us a large exciton-binding energy of about (60 meV) and the direct wide band gap (3.37 eV) at room temperature, the nanocrystals of ZnO has attracted considerable attention as a photocatalyst for the degradation of organic pollutants in water and air because of its advantage in non-toxic nature, low-cost, and high reactivity [1]. The nanocrystalline ZnO is a potential candidate in a variety of applications [2] such as optoelectronics in the short wavelength range, information storage, gas sensors [3], catalyst [4], photocatalyst [5–8], solar cells [9], luminescent material [10], and antibacterial material [11]. However, low chemical and temperature stability of the ZnO nanoparticles (dissolution to yield $Zn(OH)_2$ on the ZnO surface) and photocorrosion with release of metal ions into the environment limit the practical applications of these nanocrystalline ZnO systems [12]. In order to control the stability of the ZnO nanoparticles, colloidal solutions [13], porous glasses [14], polymers [15, 16], and alumina have been used as hosts for these metal oxide nanoparticles. Porous materials with uniform pore sizes, such as zeolites [17, 18] and mesoporous silica [19, 20], are particularly interesting as host matrices for loading metals and semiconductor nanoparticles. These supported metal oxide particles have important applications in photocatalysis and optoelectronic devices [16, 21, 22].

Nanocrystalline ZnO with different particle morphologies and sizes, as particles, clusters, layers, nanorods, nanowires, nanopellets, films, etc., can grow on internal and external surfaces of the porous supports using different methods such as chemical vapor deposition (CVD) [23–25], the vapour–liquid–solid (VLS) method [26], the sol–gel method [27, 28], and various impregnation methods [29–31], wet chemical synthesis [32], mechanochemical, and so on.

Two most common types of mesoporous silicas involve MCM-41 and SBA-15 materials. Both solids have

G. D. Mihai (✉) · N. Bilba
Materials Chemistry Laboratory, Faculty of Chemistry, "Al. I. Cuza" University of Iasi, Bvd. Carol I, no 11, 700506 Iasi, Romania
e-mail: pgdgina@yahoo.com

G. D. Mihai · V. Meynen · P. Cool · E. F. Vansant
Laboratory of Adsorption and Catalysis, University of Antwerpen (CDE), Universiteitsplein 1, Wilrijk, 2610 Antwerpen, Belgium

M. Mertens
VITO Flemish Institute for Technological Research, Boeretang 200, 2400 Antwerp, Belgium

well-ordered hexagonal porosity, thermal stability, and high surface area [33, 34]. The main difference between these materials is the size of pore diameter: SBA-15 has pores up to 300 Å and MCM-41 up to 100 Å. The well-ordered SBA-15 possesses thicker pore walls, wider pore sizes, and higher thermal and hydrothermal stability than MCM-41.

Although, methods that are based on the incipient wetness impregnation of silica matrices with zinc precursors have become popular, it is generally difficult to achieve high ZnO loadings on the host matrix and to maintain unchanged the structure of the host.

In this article, materials used in this study, with well-defined zinc oxide nanoparticles, highly dispersed on the internal and external surface of siliceous mesoporous supports, were prepared by a solvothermal impregnation method [35]. The structural ordering of all materials remains unchanged after impregnation, even at high loadings. A comparative study between structural properties of ZnO/MCM-41 and ZnO/SBA-15 materials was evaluated. The performance of these materials toward the photocatalytic degradation of dyes in aqueous solution was studied. The photocatalytic activity is in relation with their structural properties and aggregation.

Experimental procedure

Materials

The following materials were used for the preparation of the mesoporous MCM-41 and SBA-15: fumed silica (Aerosil 380, Degussa), tetraethylammonium hydroxide (20% aqueous TEAOH, Sigma Aldrich), cetyltrimethylammonium bromide (CTMABr, 99%, Acros Organics) as a surfactant for Si/MCM-41, tetraethylorthosilicate (TEOS 98% Acros Organics), HCl, and pluronics P123 ($EO_{20}PO_{70}EO_{20}$, Aldrich) as a surfactant for Si/SBA-15. For ZnO loading on the porous materials, high purity Zn (II) acetate $2H_2O$ (99%, Fluka) was used.

Synthesis

MCM-41 and SBA-15 were used as supports for the preparation of the ZnO/mesoporous silica nanocomposite materials.

The Si/MCM-41 support was synthesized from the mixture of CTMABr, TEAOH, fumed silica, and deionized water with the following molar composition $1SiO_2$: 1TEAOH:0.25CTMABr:$33H_2O$. The mixture was first stirred at 70 °C for 2 h and subsequently aged at room temperature for 24 h. The resulting gel was transferred into an autoclave and heated at 140 °C for 48 h. Then, the product was washed with fresh de-ionized water and transferred again in an autoclave heated at 140 °C for 72 h. The resultant solid was filtered, washed, and dried at ambient temperature. Finally, the solid was calcined at 550 °C for 6 h with a heating rate of 1 °C/min. Si/SBA-15 was synthesized in a similar way as that originally reported [34] by mixing the reactants having the molar composition 1TEOS:5.87HCl:$194H_2O$:0.017P123 [36]. The procedure of incorporating ZnO into the channels of these mesoporous silica is as follows: a 0.1 M Zn II acetate ethanolic solution was stirred at 70 °C for 2 h until it appeared clear and stable; the solution was stored at 20 °C to prevent growth of the particles. Afterward, the calcined silica mesoporous support materials (~0.5 g) were impregnated with different amounts of this 0.1 M Zn II acetate·$2H_2O$ ethanolic solution under vigorous stirring. Subsequently, the materials were transferred in an autoclave for aging at 80 °C until solid faces were obtained after ethanol distillation. The samples were calcined at 550 °C for 1 h (1 °C/min) in air at ambient atmosphere. In this way, ZnO/MCM-41 and ZnO/SBA-15 nanocomposites with ZnO content of up to 40.1 wt% were obtained. The final samples were denoted as *x*%ZnO/A, where *x*% = ZnO loading and A = M (MCM-41) or S (SBA-15), respectively. The resulting materials were characterized by small-angle and wide-angle X-ray diffraction (XRD), N_2 sorption, electron probe micro analysis (EPMA), and UV–Vis spectroscopy. Finally, the materials were tested as photocatalysts for the UV-induced degradation of methylene blue (MB) aqueous solution.

Characterization

X-ray powder diffraction (XRD) data were recorded on a PANanalytical X'Pert PRO diffractometer using Ni-filtered Cu K_α radiation in angular range from 1 to 6 (2θ). Measurements were done in the 2θ mode using a bracket sample holder with a scanning speed of 0.04°/4 s continuous mode.

Nitrogen adsorption/desorption isotherms were measured at −196° C in a Quantachrome Autosorb-1-MP automated gas adsorption system. Prior to measurement run, samples were outgassed under high vacuum at 200 °C for 16 h. The specific surface area was calculated on a basis of the Brunauer–Emmet–Teller (BET) method from the adsorption branch. The total pore volume of the samples was calculated from the adsorption branch of the N_2 isotherm at the $p/p_0 = 0.95$ [37] .The pore size distribution were calculated from the adsorption branch using the Barrett–Joyner–Halenda (BJH) model.

The ZnO content was determined by EPMA measurements carried out on a JEOLJXA-733 apparatus.

Diffuse Reflectance UV–vis absorption spectra were recorded on a Thermo-electron evolution 500 UV–vis

spectrometer equipped with a Thermo-electron RSA-UC40 Diffuse Reflectance cell.

The photocatalytic activity of the samples obtained was tested for the degradation of MB in aqueous solution. To a 50 mL MB solution, with initial concentration, $C_0 = 4 \times 10^{-5}$ M, 5 mg of the catalyst was added. Prior to irradiation, the solution was stirred for more than 30 min (60 min for ZnO/SBA-15 and 90 min for ZnO/MCM-41) in the darkness, to establish the adsorption–desorption equilibrium between the catalyst surface and the dye. After equilibrium, the suspension was illuminated for 1 h with UV–light (a 100 W Hg lamp, Sylvania Par 38, $\lambda = 365$ nm). The concentration of the MB dye in aqueous solution was measured at 665 nm on a Thermo-electron evolution 500 UV–Vis spectrophotometer and a calibration curve to monitor the MB concentration.

Results and discussion

Structural characterization of the ZnO/mesoporous composite materials

Loading of ZnO nanoparticles on MCM-41 (ZnO/M)

Various ZnO/MCM-41 samples were prepared using different volumes of the ethanolic 0.1 M Zn II acetate·$2H_2O$ solution. The XRD patterns in the small angle region of the parent Si–MCM-41 and of the ZnO/M samples are shown in Fig. 1.

The typical XRD pattern for Si/MCM-41 exhibits three characteristic peaks relative to the (100), (110), and (200) reflection planes corresponding to a hexagonal disposition of the channels. In all samples with low and high ZnO loadings up to 40%, the hexagonal order has remained unchanged. However, upon increase of the ZnO loading, the XRD main (100) peak become broader, and the other two have low intensity. Moreover, the peaks are shifted to higher 2θ values compared to those of the parent Si–MCM-41. The change in the relative peak intensities and the small shift to higher 2θ values suggest that ZnO is present on the internal pore walls of MCM-41[38].

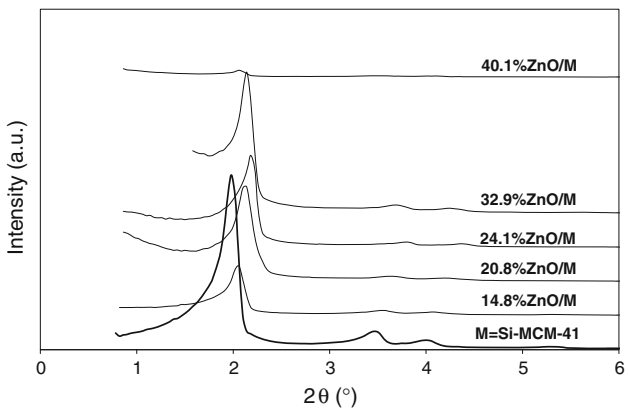

Fig. 1 Small angle XRD patterns of calcined Si/MCM-41 and of ZnO/M samples with different ZnO loadings

The adsorption/desorption isotherms of N_2 were used to study the changes in the pore structure of the ZnO/M samples upon different ZnO loadings. All the samples exhibit type IV-like isotherms according to IUPAC classifications with small hysteresis loops, characteristic to ordered mesoporous materials of the M41S family (Fig. 2a) with a narrow range of uniform and cylindrical pores.

Since isotherms are of the same type, it can be concluded that there is no structural collapse induced by the modification as was also concluded from XRD (except 40.1%ZnO/M sample). The reference material, Si–MCM-41 shows a hysteresis loop which occurs at $0.35 < p/p_0 < 0.42$ representing the spontaneous filling of the mesopores due to capillary condensation. When increasing the ZnO loading, the capillary condensation step becomes less steep due to a slightly broader pore size distribution (Fig. 2b). This could suggest that ZnO is not present in the pores as a perfectly homogeneous layer. Moreover, the capillary condensation

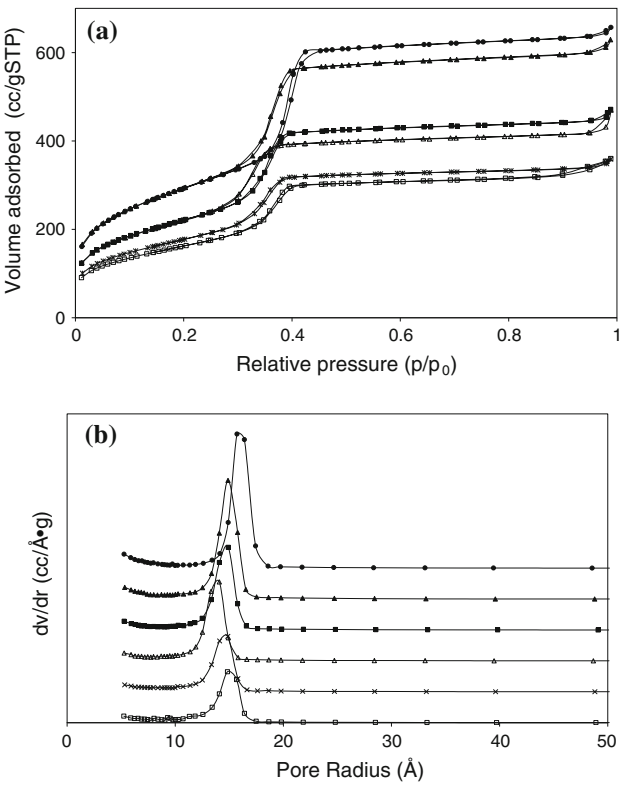

Fig. 2 Changes of N_2 isotherms (**a**) and the pore-size radius (**b**) after ZnO loadings: *filled circle* Si–MCM-41, *filled triangle* 14.8%ZnO/M, *filled square* 20.8%ZnO/M, *open triangle* 24.1%ZnO/M, *cross* 32.9%ZnO/M, and *open square* 40.1%ZnO/M

step is shifted to lower relative pressure p/p_0 confirming the narrowing of the pores to smaller pore sizes compared to the parent Si–MCM-41. This observation is in agreement with the XRD results (the peaks shift to higher 2θ values). Furthermore, a decrease of the BET surface area and the total pore volume (Table 1) with increasing zinc oxide loading indicate the presence of some mesopore blocking by the ZnO particles, leading to the decrease of the uniformity and the ordering of the mesoporous structure. Similar trend was observed by Wu et al. [39] after impregnation of SBA-15 with MoO_3 and Busuioc et al. [36] by incorporation of TiO_2 in SBA-15 and MCM-41.

Figure 3 displays the high-angle XRD patterns of ZnO–MCM-41 with different ZnO contents, along with the XRD pattern of standard wurtzite ZnO (space group $P6_3mc$) with the lattice constants $a = b = 3.249$ Å and $c = 5.206$ Å, and a c/a ratio of 1.602. For samples with high loadings of ZnO (>32%), all diffraction peaks are similar to those of bulk ZnO confirming the hexagonal wurtzite structure.

XRD patterns for these samples show nine distinct peaks at $2\theta = 31.7°$, 34.36°, 36.2°, 47.54°, 56.6°, 62.76°, 66.34°, 68.82°, and 69.3°, corresponding to the reflection from (100), (002), (101), (102), (110), (103), (200), (112), and (201) planes, respectively (JCPDS 5-664). No characteristic peaks from impurities were observed in the samples which mean that the crystals were composed of a pure ZnO phase. The ZnO nanoparticles could not be detected in the case of the samples with low ZnO loadings (14.8, 20.8, and 24.1%); in this case, the nanoparticles will be too small or amorphous. For all the materials with higher loadings that do show a crystalline phase, it was found that the ZnO particles have a preferential orientation along the (101) plane, as this peak has the highest intensity. Therefore, the crystallite sizes of the particles (D_{XRD}) were determined using the diffraction peak of the (101) ZnO plane and the Scherrer's equation: $D_{crystal} = (0.89\ \lambda)/(\beta \cos \theta)$, where λ is the X-ray wavelength of incident X-rays ($\lambda_{Cu} = 0.154$ nm), β is the full width at half-maximum intensity of (101) peak and θ is the diffraction angle (Table 1). The calculated average crystallite size of ZnO exceeds the Si–MCM-41 mesopore size (~3 nm). Therefore, those nanoparticles should be located on the external surface of the support. Although some particles are outside, a substantial amount of ZnO will also be present at the internal surface, causing a reduction in the pore size as was observed with N_2-sorption and low angle XRD. However, it can be assumed that the internal ZnO phase consists of small (<3 nm) particles below the detection limit of the XRD. The trend in the XRD patterns (Fig. 3) suggests that the contribution of the external phase will increase upon higher loadings (starting at around 32% of ZnO). In the XRD diffractograms of 14.8%ZnO, 20.8%ZnO, and 24.1%ZnO, the diffraction peaks of ZnO phase have not been observed in accordance with the published results [40]. The ZnO is highly dispersed inside the mesopores of MCM-41.

Table 1 Structural characteristics of ZnO/M samples with different ZnO loadings and siliceous MCM-41

Sample	ZnO (wt%)	S_{BET} (m^2/g)	TPV (cc/g)	D_p (nm)	D_{ZnO} (nm)
Si/MCM-41	–	1070	0.98	3.14	–
14.8%ZnO/M	14.8	1070	0.93	2.97	–
20.8%ZnO/M	20.8	808	0.69	2.98	–
24.1%ZnO/M	24.1	811	0.65	2.82	–
32.9%ZnO/M	32.9	651	0.53	2.97	21.7
40.1%ZnO/M	40.1	599	0.53	2.97	21.69

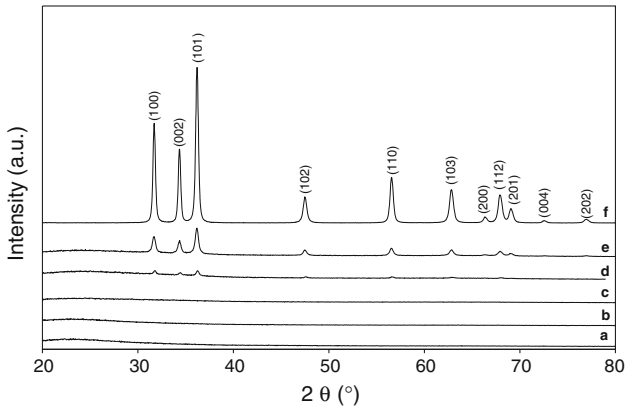

Fig. 3 Wide-angle XRD patterns for the x%ZnO/M samples: (*a*) 14.8%ZnO, (*b*) 20.8%ZnO, (*c*) 24.1%ZnO, (*d*) 32.9%ZnO, (*e*) 40.1%ZnO, and (*f*) pure ZnO

Figure 4 shows the UV–vis Diffuse Reflectance absorption spectra of parent Si/MCM-41, ZnO/M samples with different ZnO loadings, and of crystalline bulk ZnO as reference sample. The pure siliceous MCM-41 gives very little absorption in this range. The bulk ZnO powders show a strong absorption below 400 nm with an absorbance peak between 370 and 330 nm. Bulk crystalline ZnO starts to absorb near 370 nm [41]. However, the wavelengths absorption spectra of nanocrystalline ZnO powder supported on MCM-41 are usually blue shifted to lower values (at around 360 nm) due to the well-known quantum size effect [42]. In general, this phenomenon is observed for very small particle size (<5 nm) [43].

The absorption spectra for the samples with ZnO loadings >14.8% gives an absorption band between 240 and 400 nm which confirms the existence of a mixture of nanoparticles with different particle size on the MCM-41 surface and corresponds well with the XRD patterns. An absorption band is observed for the samples with 20.8%

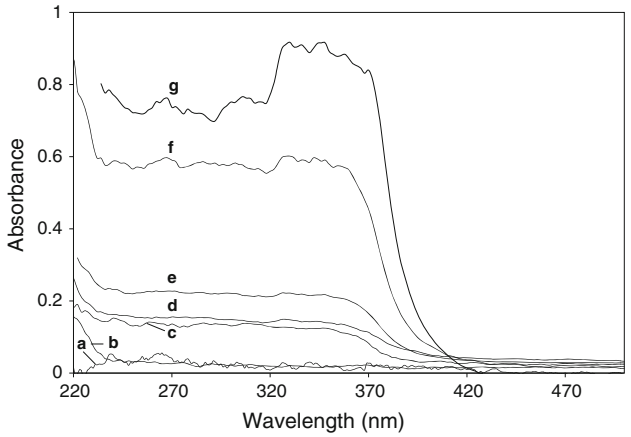

Fig. 4 Diffuse Reflectance UV–vis spectra for parent Si/MCM-41, ZnO/M samples synthesized with different ZnO loadings and pure ZnO: (*a*) Si/MCM-41, (*b*) 14.8%ZnO, (*c*) 20.8%ZnO, (*d*) 24.1%ZnO, (*e*) 32.9%ZnO, (*f*) 40.1%ZnO, and (*g*) pure ZnO

ZnO and 24.1% ZnO loadings, although the crystalline ZnO phase was not detected in XRD. This suggests that the crystal sizes at these loadings are very small (below the detection limit of the XRD). The UVDR spectra revealed that the intensity of the absorption band increases with increasing ZnO loading. For 14.8%ZnO/M the absorption band is not observed, indicating that no crystalline ZnO phase exists, as was observed in the high angle XRD pattern. Therefore, when these low loadings are obtained, only a very much dispersed ZnO phase can be observed (absorption edge at around 240 nm) [30, 44]. This single layer of ZnO is probably located on the internal surface of the MCM-41 phase causing the reduction of the pore diameter. Since the absorption edge at 240 nm can also be observed at higher loadings and similar reductions in the pore diameter are also observed at these high loadings, it can be suspected also that at high loadings, some amorphous phase is present at the internal pore structure.

Loading of ZnO nanoparticles on SBA-15 (ZnO/S)

The ZnO/S samples with different ZnO loadings were prepared in the same way as for the ZnO/M samples. The chemical and physical properties of the ZnO/S samples are compiled in Table 2. Compared to MCM-41, SBA-15 exhibits a much larger pore size (Table 2).

Figure 5 illustrates the XRD patterns of ZnO/S samples along with parent Si–SBA-15.

The SAXRD patterns of the ZnO/S samples modified with ZnO exhibit three peaks corresponding to reflections of (100), (110), and (200) planes of a 2D hexagonally ordered structure of the SBA-15. Therefore, after impregnation the introduction of ZnO did not affect the hexagonal pore

Table 2 Structural characteristics of ZnO/S samples with different ZnO loadings and of parent Si–SBA-15

Sample	ZnO (wt%)	S_{BET} (m^2/g)	TPV (cc/g)	Dp (nm)	D_{ZnO} (nm)
Si–SBA-15	–	521	0.6	6.36	–
16.8%ZnO/S	16.8	370	0.503	6.02	–
23.6%ZnO/S	23.6	328	0.45	6.00	–
38.1%ZnO/S	38.1	251	0.42	6.08	16.53

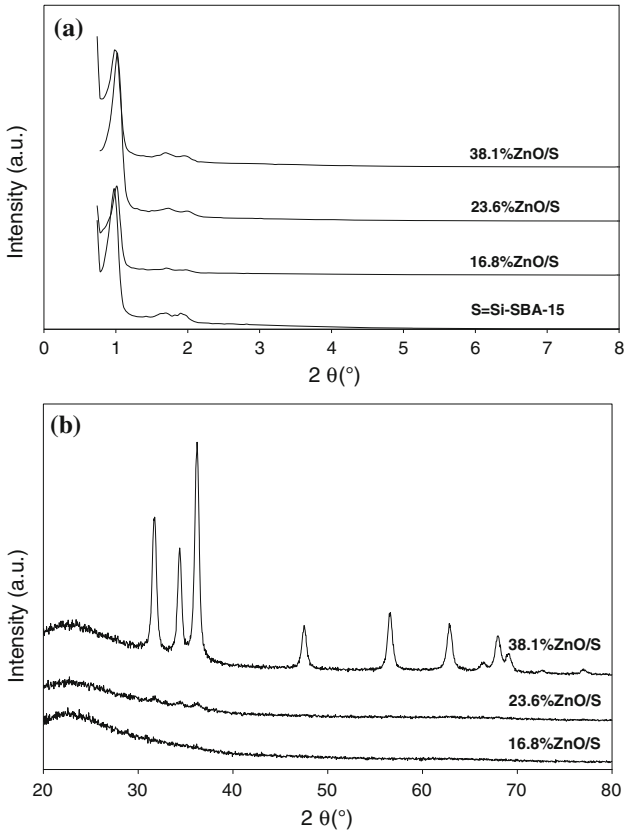

Fig. 5 Small-angle XRD patterns of SBA-15, before and after impregnation with different ZnO loadings (**a**) and wide angle XRD pattern of ZnO/S samples with different ZnO loading (**b**)

structure of SBA-15. The high-angle XRD patterns (Fig. 5b) demonstrate that when ZnO loadings were equal or above 23.6 wt%, ZnO nanocrystallite began to appear. Since the size of the ZnO nanocrystallites at high loadings (16.53 nm) is larger than the pore size (~6 nm) (Table 2), it can be concluded that in the case of the highest ZnO loading (38.1%), ZnO crystals might have been formed on the external surface.

Figure 6 illustrates the N_2-adsorption–desorption isotherms of SBA-15 before and after impregnation with the

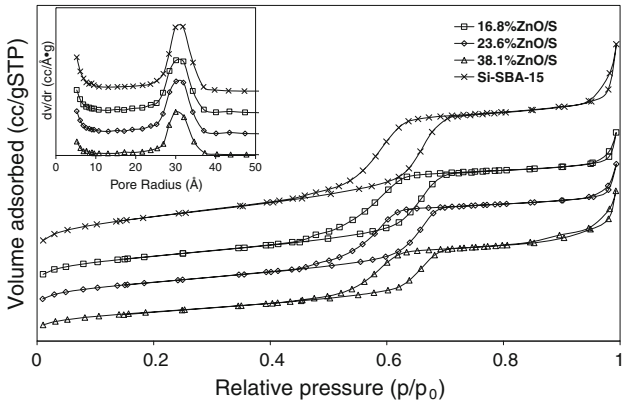

Fig. 6 N_2 adsorption–desorption isotherms of SBA-15 before and after impregnation with different ZnO loadings. *Inset* is pore size distribution

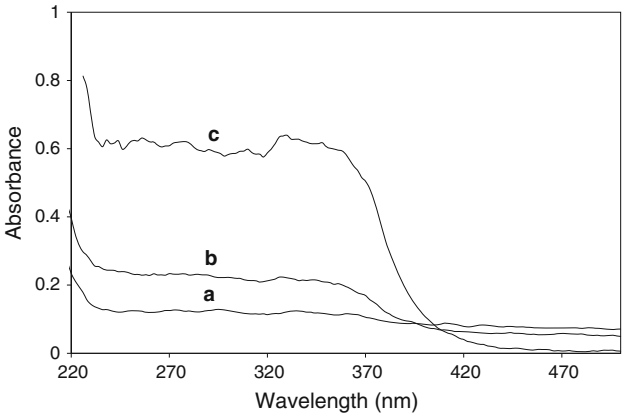

Fig. 7 Diffuse Reflectance UV–vis spectra for the ZnO/S samples synthesized with different ZnO loadings: (*a*) 16.8%ZnO, (*b*) 23.6%ZnO, and (*c*) 38.1%ZnO

Zn II acetate·$2H_2O$ solution. ZnO/S samples display a type IV isotherm and exhibit a H_1 hysteresis loop purely as siliceous mesoporous SBA-15.

The sharpness of the inflection step decreased with increasing ZnO loading, and also the pore size distribution is slightly shifted toward lower values.

After impregnation with ZnO, the surface area, the total pore volume, and the micropore volume are decreased (Table 2). The decrease in surface area can be explained by partial filling of the mesopores and mostly the micropores with ZnO. However, the decrease in porous characteristics is less severe as in the case of MCM-41 as the support. Moreover, no evidence for plugs or ink bottle pores was detected in the hysteresis loop. This indicates that when ZnO is deposited on supports with larger pore diameters, pore blocking is avoided on loading with high amounts of ZnO. Since in XRD (Fig. 4), the first reflection peak of SBA-15 (100) was not shifted to higher values 2θ after deposition of the ZnO nanoparticles, the decrease in pore diameter of the ZnO/S materials indicates that the pore walls became thicker. Therefore, it can be assumed that part of the ZnO phase has been deposited as a quite homogeneous layer on the internal surface of the SBA-15 support [45].

UVDR spectra of ZnO/S samples shows the same trend as was observed for the ZnO/M samples (Fig. 7). Starting with the lowest ZnO loading (16.8%), the absorption edge can be found at around 240 nm indicative of an amorphous ZnO phase.

In ZnO/S materials, ZnO crystals started to form at lower percent of ZnO (23.6%) compared to the ZnO/M case where the crystals are observed at 32.9% ZnO. A possible explanation could be the lower surface area of the ZnO/S materials in contrast to the ZnO/M materials. Therefore, the surface will be saturated at much lower loadings resulting in the formation of crystalline phases at lower amounts of ZnO. In the UVDR spectra, both ZnO/M and ZnO/S materials present an amorphous and a crystalline ZnO phase shown by an absorption band in the region 240-500 nm.

Photocatalytic activity of ZnO/mesoporous materials

Owing to its electrical and optical properties, ZnO has been evaluated as a good semiconductor-type photocatalyst for the degradation of pollutants from aqueous solutions [6, 46].

Processes including photocatalysis systems are a combination of a semiconductor (TiO_2, ZnO, etc.), and UV light. When the ZnO nanoparticles are irradiated under UV light (supraband gap photons) of wavelength less than 400 nm (greater than that of the band gap, E_g, eV), the electrons of the valence band will be excited by the absorbed energy of the UV ray and jump to conduction band ($e^-_{c.b.}$); at the same time, the valence band will create electric holes carrying positive electricity ($h^+_{v.b.}$). The general pairs, electrons and holes (EHPs) are considered the main species involved in the sensitized photocatalytic vibration process. The energy required of a photon to generate an EHP in a photocatalyst can be related to the wavelength, λ, as given by the following equation: $\lambda \leq 1240/E_g$, where E_g is the band gap of semiconductor, eV.

In a heterogeneous photocatalytic process, photoinduced chemical reactions occur at the surface of a catalyst producing the highly reactive radicals, $^{\bullet}OH$ and $^{\bullet}O_2^-$ that can oxidize organic compounds. The possible reaction scheme for the photocatalytic degradation of organic compounds is given below:

$$ZnO + h\upsilon \rightarrow ZnO^{*}\left(e^{-}_{c.b.} + h^{+}_{v.b.}\right)$$

[generation of an EHP];

$$ZnO^{*}\left(e^{-}_{c.b.EHP} + h^{+}_{v.b.}\right) \rightarrow ZnO + \text{heat}$$

[recombination in volume];

$$h^{+}_{v.b.} + H_2O \rightarrow HO^{\bullet} + H^{+}$$

$$h^{+}_{v.b.} + HO^{-} \rightarrow HO^{\bullet} \text{ hydroxyl radical}$$

$$e^{-}_{c.b.} + O_2\text{ads} \rightarrow {}^{\bullet}O_2^{-} \text{ superoxide radical}$$

$$HO^{\bullet} + \text{MB (organics)} \rightarrow \text{intermediates} + \text{mineral salts} \rightarrow CO_2,\ H_2O,\ \text{etc.}\quad \text{[oxidation]}.$$

The parameters that affect the photocatalytic activity include the catalyst, band gap, surface area, porosity, crystal structure, crystallinity, purity, density of surface, hydroxyl groups, e^{-} and h^{+} migration characteristics, surface acidity, and size distribution.

In this study, the adsorption behavior of methylene blue, a cationic basic dye, on the supports with the highest ZnO loading is explored prior to the photocatalytic tests. The adsorption kinetics of MB on Si–MCM-41, Si-SBA-15, and pure ZnO were recorded. It was found that the adsorption–desorption equilibrium between the catalyst surface and the dye was different for the various supports. For the bulk ZnO pHzpc of 9.0), the adsorption of MB is null, but for Si–SBA-15 and ZnO/S, the equilibrium is reached within 10 min of time. For the Si–MCM-41 and ZnOM samples, this equilibrium is set after longer exposure times (60 min) due to the porous characteristics of MCM-41 materials. Since ZnO is not porous and SBA-15 has much larger pores in comparison to MCM-41, diffusion effects have less influence on the adsorption–desorption equilibrium. The smaller mesopores of MCM-41, on the other hand, allow only slow diffusion of the MB (with molecular diameter of 0.941 nm [47]) into the pores of MCM-41. After deposition with the highest loadings of ZnO, a clear difference arises between the SBA-15 and MCM-41 materials. The results show (Fig. 8a) a slower adsorption of MB on ZnO/M photocatalysts in comparison to purely siliceous MCM-41.

In the case of MCM-41, the adsorption–desorption equilibrium is much slower after ZnO deposition. Deposition on SBA-15, on the other hand, does not prolong the equilibrium time. As discussed above, the pore diameter of the MCM-41 materials has decreased to values of about 2.9 nm. Also, the surface area has decreased intensively (Table 1) which indicates the presence of some pore blocking effects. In the SBA-15 materials, the diameter of the pores remains relatively large (6 nm) compared to MCM-41 (2.9 nm) after deposition, and no pore blocking effects were present. Therefore, it can be assumed that after deposition with ZnO, the diffusion of the dye to the internal surface is even more retarded in the case of MCM-41.

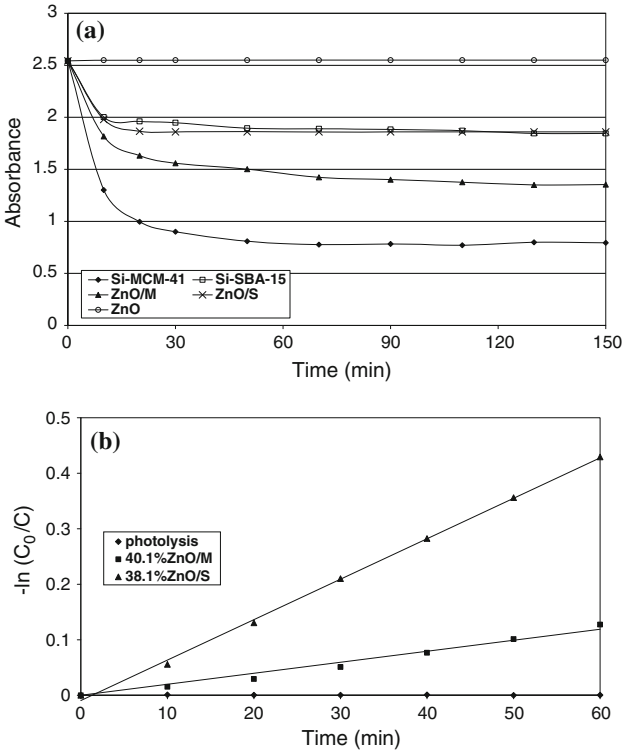

Fig. 8 **a** Adsorption behavior of methylene blue on MCM-41 and SBA-15 before and after impregnation with ZnO and pure ZnO and **b** catalytic rates of ZnO/M and ZnO/S for photocatalytic degradation of methylene blue

The amount of MB adsorbed on the surface of the different catalysts showed the order of sequence: MCM-41 > SBA-15 > ZnO which can be directly related to the surface area which is available for adsorption.

In order to demonstrate the potential applicability of the ZnO/mesoporous materials, the photocatalytic activity of these catalysts was evaluated by measuring the degradation of MB in water under ultraviolet illumination. The MB decolorization in the absence of catalyst (photolysis) was also evaluated to verify that the color removal of MB was indeed due to the photocatalytic process. The photodegradation of MB by ZnO follows a first-order kinetics: $-\ln(c_0/c) = kt$, where c_0 is the equilibrium concentration of MB in the solution. The experiment conducted in the absence of the photocatalyst but under UV light demonstrated that the MB could not be degraded. The photocatalytic activities of ZnO/M and ZnO/S are compared and seem to depend on the type of supports used.

Figure 8b shows the catalytic rates as a function of time of the supported ZnO materials deposited on SBA-15 and MCM-41 after adsorption–desorption equilibrium was reached.

It can be clearly seen that ZnO/S shows photocatalytic activity; ZnO/M, on the other hand, shows almost no

photocatalytic activity. A low photocatalytic activity is somewhat expected since the samples contain two types of ZnO phase; one, crystalline phase on the external surface of the supports which is photocatalytic active, and the other an amorphous phase, which forms an inactive spread layer on the internal pore. It is well known that factors, such as crystal phase, crystal size, and concentration of active elements in the crystal phase, etc., play an important role in influencing the photocatalytic activity. In general, smaller particles offer a high number of active sites per unit of mass which act as centres for the photocatalytic reactions [34]. This explains the higher activity for sample ZnO/S which has smaller particles than the sample ZnO/M. Moreover, the kinetics of adsorption are much faster on ZnO/S, and no pore blocking effects were observed in contrast to the ZnO/M materials.

Conclusions

Structural, surface, and adsorption/photocatalytic properties were compared for ZnO loaded on different mesoporous materials (MCM-41 and SBA-15) obtained through an impregnation method with a non-aqueous $Zn(ac)_2$ solution.

High ZnO loadings (up to 38%) can be achieved on the host materials without degradation of the structural properties of the support material, even when high loadings are applied. The information acquired by XRD, nitrogen adsorption–desorption and UV-Diffuse Reflectance techniques demonstrate that ZnO is present in both crystalline and amorphous phases. In both cases, next to the crystals, there is also an amorphous phase present on the internal pore walls, being responsible for the narrowing of the pores. Compared to MCM-41, SBA-15 mesoporous structure remains almost intact even after introduction of significant amounts of ZnO. The size of the nanoparticles depends on the type of support that is used.

In summary, the adsorption–desorption equilibrium between the photocatalysts and MB was found to be strongly dependent on the porous properties of the photocatalyst. The long adsorption times recorded to reach equilibrium, indicate that adsorption–desorption equilibriums should always be taken when performing photocatalytic test reactions with large molecules and porous materials. A higher photocatalytic activity was found for ZnO/S in comparison to ZnO/M sample, owing to the smaller crystal size of ZnO and the porous characteristics of SBA-15.

Acknowledgments This study is part of the NoE project "Inside Pores" and the GOA project funded by the Special Fund for Research of the University of Antwerp. V. Meynen acknowledges the financial support received from FWO-Flanders (Fund for Scientific Research).

References

1. Driessen MD, Miller TM, Grassian VH (1998) J Mol Catal A Chem 131:149
2. Pearton SJ, Norton DP, Ip K, Heo YW, Steiner T (2005) Prog Mater Sci 580:293
3. Zhang Q, Xie C, Zhang S, Wang A, Zhu B, Wang L, Yang Z (2005) Sens Actuators B 110:370
4. Huang WJ, Fang GC, Wang CC (2005) Colloid Surf A Physicochem Eng Aspects 260:45
5. Amapoorani R, Dhangeyan MR, Renganathan RJ (1997) Photochem Photobiol A Chem 111:215
6. Ullah R, Dutta J (2008) J Hazard Mater 156:194
7. Carlos AK, Wypych GF, Moraes SG, Duran N, Nagata N, Peralta PZ (2000) Chemosphere 40:433
8. Byrappa K, Dayananda AS, Sajan CP, Basavalingu B, Shayan MB, Soga K, Yoshimura M (2008) J Mater Sci 43:2348. doi: 10.1007/s10853-007-1989-8
9. Matsubara K, Fons P, Iwata K, Yamada A, Sakurai K, Tampo H, Niki S (2003) Thin Solid Films 431:369
10. Zhang J, Yu W, Zhang L (2002) Phys Lett A 299:276
11. Sanches L, Peral J, Domenech X (1996) Electrochim Acta 41:1981
12. Jin XH, Gao L (2001) J Inorg Mater 16:200
13. Rossetti R, Hull R, Gibson JM, Brus LE (1985) J Chem Phys 83:1406
14. Ekimov AI, AlL Efros, Onushcenko AA (1985) Solid State Commun 56:921
15. Abdullah M, Morimoto T, Okuyama K (2003) Adv Funct Mater 13:800
16. Ji LW, Shih WS, Fang TH, Wu CZ, Peng SM, Meen TH (2010) J Mater Sci 45:3266. doi:10.1007/s10853-010-4336-4
17. Chen J, Feng Z, Ying P, Li C (2004) J Phys Chem B 108:12669
18. Bovy C, Marine W, Sporken R, Su BL (2007) Colloids Surf A 300:145
19. Lu QS, Wang ZY, Li JG, Wang P, Ye X (2009) Nanoscale Res Lett 4:646
20. Jiang Q, Wu ZY, Wang YM, Cao Y, Zhou CF, Zhu JH (2006) J Mater Chem 16:1536
21. Topka P, Balcar H, Rathouskỳ J, Žilková N, Verpoort F, Čejka (2006) J Microporous Mesoporous Mater 96:44
22. Chakrabarti S, Dutta BK (2004) J Hazard Mater B 112:269
23. Matsumoto K, Konemura K, Shimaoka G (1988) J Cryst Growth 71:99
24. Matsumoto K, Shimaoka G (1985) J Cryst Growth 86:410
25. Li YJ, Duan R, Shi PB, Qin GG (2004) J Cryst Growth 260:309
26. Huang M, Wu Y, Feick H, Tran N, Weber E, Yang P (2001) Adv Mater 13:113
27. Cheng HM, Hsu HC, Chen SL, Wu WT, Kao CC, Lin LJ, Hsieh WF (2005) J Cryst Growth 277:192
28. Dai WL, Cao Y, Ren LP, Yang XL, Xu JH, Li HX, He HY, Fan KN (2004) J Catal 229:80
29. Zhang W, Shi J, Wang L, Yan D (2000) Chem Mater 12:1408
30. Schröder F, Hermes S, Parala H, Hikov T, Muhler M, Fischer RA (2006) J Mater Chem 16:3565
31. Burova LI, Petukhov DI, Eliseev AA, Lukashin AV, Tretyakov YD (2006) Superlattices Microstruct 39:257
32. Zeng W, Wang Z, Qian XF, Yin J, Zhu ZK (2006) Mater Res Bull 41:1155
33. Kresge CT, Leonowicz ME, Roth WJ, Vartuli JC, Beck JS (1992) Nature 359:710
34. Zhao DY, Feng JL, Huo QS, Melosh N, Fredrickson GH, Chmelka BF, Stucky GD (1998) Science 279:548
35. Xiong Y, Zhang LZ, Tang GQ, Zhang GL, Chen WJ (2004) J Lumin 110:17

36. Busuioc AM, Meynen V, Beyers E, Mertens M, Cool P, Bilba N, Vansant EF (2006) Appl Catal A 312:153
37. Barret E, Joyner L, Halenda P (1951) J Am Chem Soc 73:373
38. Sauer J, Marlow F, Schüth F (2001) Phys Chem Chem Phys 3:5579
39. Wu PY, Ji SF, Hu LH, Zhu JQ, Li CY (2008) J Porous Mater 15:181
40. Lu W, Lu G, Luo Y, Chen A (2002) J Mol Catal A Chem 188:225
41. Bahnemann DW, Kormann C, Hoffmann MR (1987) J Phys Chem 91:3789
42. Ramakrishna G, Ghosh HN (2003) Langmuir 19:3006
43. Wong E, Searson P (1999) Appl Phys Lett 74:2939
44. Bickley RI, Stone FS (1973) J Catal 31:389
45. Yang HF, Lu QY, Gao F, Shi QH, Yan Y, Zhang FQ, Xie SH, Tu B, Zhao DY (2005) Adv Funct Mater 15:1377
46. Wang H, Xie C, Zhang W, Cai S, Yang Z, Gui Y (2007) J Hazard Mater 141:645
47. Weng CH, Pan YF (2006) Colloids Surf A 274:154